Journal of Materiomics 8 (2022) 1095–1103

Contents lists available at ScienceDirect

Journal of Materiomics

journal homepage: www.journals.elsevier.com/journal-of-materiomics/

High-performance and stable $AgSbTe_2$-based thermoelectric materials for near room temperature applications

Yi Wu [a, b], Pengfei Qiu [a, b, *], Yuan Yu [c, **], Yifei Xiong [a, b, c], Tingting Deng [d], Oana Cojocaru-Mirédin [c], Matthias Wuttig [c, e], Xun Shi [a, b], Lidong Chen [a, b]

[a] State Key Laboratory of High Performance Ceramics and Superfine Microstructure, Shanghai Institute of Ceramics, Chinese Academy of Sciences, Shanghai, 200050, China
[b] Center of Materials Science and Optoelectronics Engineering, University of Chinese Academy of Sciences, Beijing, 100049, China
[c] Institute of Physics (IA), RWTH Aachen University, Aachen, 52056, Germany
[d] School of Chemistry and Materials Science, Hangzhou Institute for Advanced Study, University of Chinese Academy of Sciences, Hangzhou, 310024, China
[e] Peter Grünberg Institute—JARA-Institute Energy-Efficient Information Technology (PGI-10), Forschungszentrum Jülich GmbH, Jülich, 52428, Germany

ARTICLE INFO

Article history:
Received 14 June 2022
Received in revised form
11 July 2022
Accepted 12 July 2022
Available online 20 August 2022

ABSTRACT

$AgSbTe_2$-based ternary chalcogenides show excellent thermoelectric performance at low- and middle-temperature ranges, yet their practical applications are greatly limited by their intrinsic poor thermodynamic stability. In this work, we demonstrate that $AgSbTe_2$-based ternary chalcogenides can be stabilized for service below their decomposition threshold. A series of $Ag_xSb_{2-x}Te_{3-x}$ ($x = 1.0, 0.9, 0.8$ and 0.7) samples have been prepared by the melt-quenching method. Among them, phase pure $Ag_{0.9}Sb_{1.1}Te_{2.1}$ is verified by comprehensive structural characterizations from macroscale by X-ray diffraction to microscale by energy-dispersive spectroscopy and then to sub-nanometer scale by atom probe tomography. This composition is further chosen for the stability investigation. The decomposition threshold of $Ag_{0.9}Sb_{1.1}Te_{2.1}$ appears around 473 K. Below this temperature, the chemical compositions and thermoelectric properties are barely changed even after 720 h annealing at 473 K. The figure-of-merit (zT) value of $Ag_{0.9}Sb_{1.1}Te_{2.1}$ below the decomposition threshold is very competitive for real applications even compared with Bi_2Te_3-based alloys. The average zT of $Ag_{0.9}Sb_{1.1}Te_{2.1}$ at 300–473 K reaches 0.84, which is higher than most other thermoelectric materials in a similar temperature range, promising applications in miniaturized refrigeration and power generation near room temperature.

1. Introduction

Thermoelectric (TE) materials can directly convert the low-grade waste heat into useful electricity [1,2]. The heat to electricity conversion efficiency is determined by the dimensionless figure-of-merit zT of materials, which is defined as $zT = S^2\sigma/\kappa T$, where S is the Seebeck coefficient, σ is the electrical conductivity, κ is the thermal conductivity, and T is the absolute temperature [3,4]. The past decades have witnessed considerable success in improving the zT of TE materials [5–9]. However, many high-zT materials exhibit obvious weakness in stability (*e.g.* oxidation [10], elemental volatility [11], ion migration [12], and phase transition [13]), which greatly limits their range of practical applications.

$AgSbTe_2$-based TE chalcogenides show excellent zT in the low- and middle-temperature range (300–600 K) [14]. Stoichiometric $AgSbTe_2$ adopts a cubic rock salt structure ($Fm\,\bar{3}\,m$), where Ag, Sb, and vacancies randomly occupy the 4a sites while Te atoms occupy the 4b sites (Fig. 1a) [15]. It has been recently demonstrated that $AgSbTe_2$ is an incipient metal employing an unconventional chemical bonding mechanism, coined metavalent bonding (MVB) [16–20]. This bonding mechanism is responsible for the moderate band gap (around 0.3 eV) [21], multiple degenerate valence bands [22], and an ultralow lattice thermal conductivity [23,24], which are all beneficial factors for thermoelectrics. The TE performance of $AgSbTe_2$ was firstly reported in the late 1950s [25,26]. Yet, it attracted extensive attention from the TE community till the first

* Corresponding author. State Key Laboratory of High Performance Ceramics and Superfine Microstructure, Shanghai Institute of Ceramics, Chinese Academy of Sciences, Shanghai, 200050, China.
** Corresponding author.
E-mail addresses: qiupf@mail.sic.ac.cn (P. Qiu), yu@physik.rwth-aachen.de (Y. Yu).
Peer review under responsibility of The Chinese Ceramic Society.

https://doi.org/10.1016/j.jmat.2022.07.005

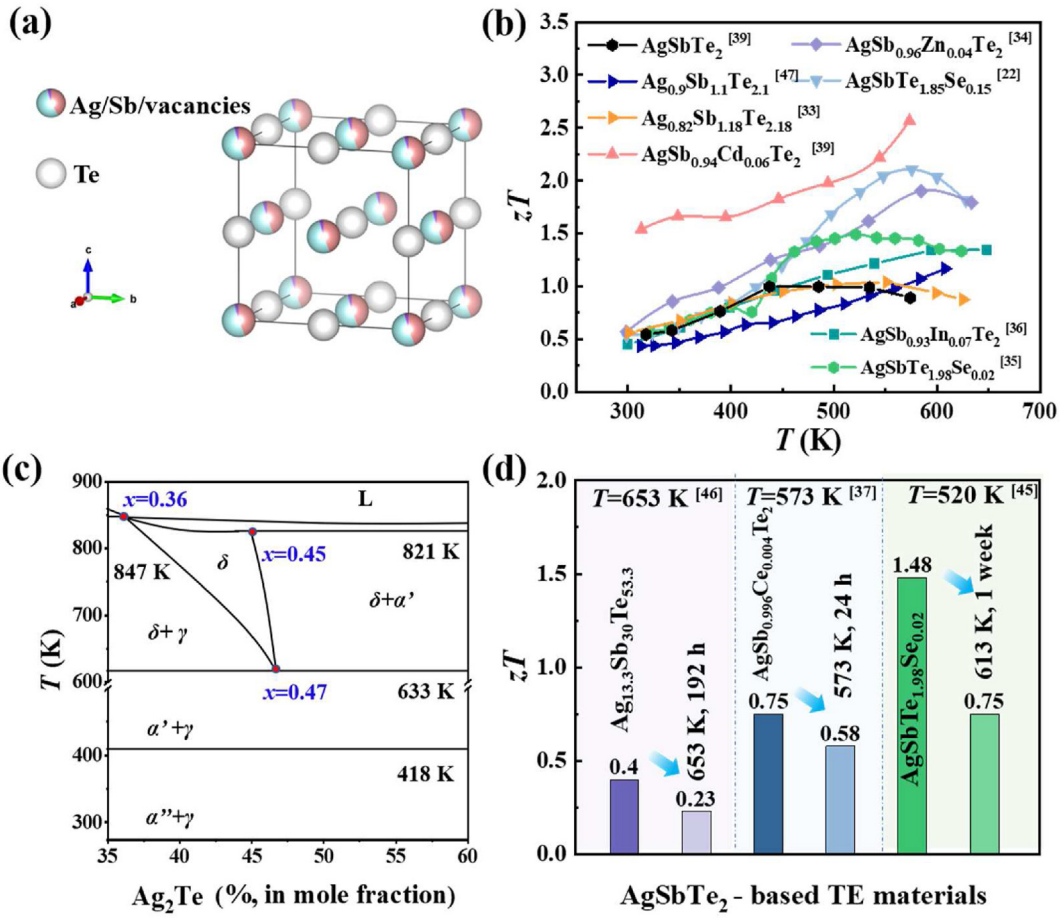

Fig. 1. (a) Schematics of the crystal structure of $AgSbTe_2$ cubic δ-phase. (b) Reported TE figure-of-merit (zT) of typical $AgSbTe_2$-based ternary chalcogenides [22,33–36,39,47]. (c) Ag_2Te-Sb_2Te_3 pseudobinary phase diagram proposed by Petzow *et al.* [40,41]. 'α'''', 'α''', and 'γ' represent the monoclinic Ag_2Te phase, cubic Ag_2Te phase, and Sb_2Te_3 phase, respectively. (d) zT of several $AgSbTe_2$-based ternary chalcogenides before and after annealing at assigned temperature [37,45,46].

decade of the 21st century [27–29]. The peak zT of stoichiometric $AgSbTe_2$ ranges from 0.8 to 1.5, sensitively depending on the fabrication method [30–32]. Upon introducing non-stoichiometry [33] or exotic dopants (*e.g.* Zn [34], Se [35], In [36], Ce [37], Sn [38], and Cd [39]), the zT can be enhanced to as high as 2.6, which is among the highest values reported in thermoelectrics (Fig. 1b).

Despite the high zTs, the $AgSbTe_2$-based ternary chalcogenides are metastable. Based on the Ag_2Te-Sb_2Te_3 pseudo-binary phase diagram proposed by Petzow *et al.* (Fig. 1c) [40,41], stable $AgSbTe_2$, which is usually named the δ-phase, only exists in a narrow chemical composition range with a chemical formula of $Ag_xSb_{2-x}Te_{3-x}$ ($0.72 < x < 0.94$) and a small temperature window (633–847 K). Below 633 K, the cubic δ-phase will decompose into Ag_2Te/Sb_2Te_3 mixtures after experiencing a eutectoid transformation. Interestingly, the metastable cubic δ-phase can still be obtained at room temperature [39,42,43], but it will partially decompose into Ag_2Te/Sb_2Te_3 mixtures upon heating. For example, Wu *et al.* annealed $AgSbTe_2$ at 523 K for 12 960 h and found it completely decomposed into the Ag_2Te/Sb_2Te_3 mixtures [44]. A similar phenomenon was also observed by Wyżga *et al.* after annealing $AgSbTe_2$ at the same temperature for 1 month [45]. Cojocaru-Mirédin *et al.* annealed $Ag_{16.6}Sb_{30}Te_{53.3}$ at 653 K for 192 h and found it partially decomposed into $(Ag,Sb)_2Te_3$. Such poor stability leads to the inferior reproducibility of the TE properties [46]. Wyżga *et al.* found the S of $Ag_{0.9}Sb_{1.1}Te_{2.1}$ gradually changed from 346 $\mu V \cdot K^{-1}$ to 195 $\mu V \cdot K^{-1}$, while the σ changed from 0.7×10^4 $S \cdot m^{-1}$ to 3.0×10^4 $S \cdot m^{-1}$ at 310 K during the cycling test between 300 K and 650 K [47]. Schmidt *et al.* found that the zT of $AgSbTe_{1.98}Se_{0.02}$ at 520 K decreased from 1.48 to 0.75 after annealing at 613 K for 1 week (Fig. 1d) [45]. Lee *et al.* found that the zT of Ce-doped $AgSbTe_2$ at 573 K increased from 0.75 to 1.28 after annealing at 673 K for 24 h, and then decreased to 0.58 after annealing at 573 K for 24 h (Fig. 1d) [37].

Developing stable $AgSbTe_2$-based ternary chalcogenides has become the foremost task for achieving practical applications. In this work, a series of $Ag_xSb_{2-x}Te_{3-x}$ ($x = 1.0$, 0.9, 0.8 and 0.7) samples have been prepared. Among them, only $Ag_{0.9}Sb_{1.1}Te_{2.1}$ (note that this composition contains cation vacancies rather than anion interstitials) is found to be phase pure without obvious secondary phases at room temperature. We thus choose this composition to study its phase decomposition behavior to avoid the detrimental impact of secondary phases. The corresponding decomposition threshold temperature is determined to be around 473 K. Below this threshold, its chemical compositions and TE properties are barely changed after long-term annealing at 473 K for 720 h. Particularly, below 473 K, $Ag_{0.9}Sb_{1.1}Te_{2.1}$ shows superior zT to most other typical TE materials. Our work uncovers the composition and temperature regime for the stable and durable application of $AgSbTe_2$-based ternary chalcogenides.

2. Method

Polycrystalline $Ag_xSb_{2-x}Te_{3-x}$ (x = 1.0, 0.9, 0.8 and 0.7) samples were synthesized by melt-quenching method. High-quality elements, Ag (Alfa, 99.99%), Sb (Alfa, 99.99%), and Te (Alfa, 99.99%) were weighed out according to the stoichiometry and sealed in the quartz tubes with a high vacuum (~10^{-4} Torr). The tubes were heated to 723 K in 12 h, kept at this temperature for 6 h, and then heated to 1173 K in 4.5 h. After preserving at 1173 K for 6 h, the tubes were cooled to 725 K in 6 h and kept at this temperature for 2 d. Finally, the tubes were quenched to room temperature. The ingots were crushed into fine powders and then consolidated by spark plasma sintering (Sumitomo, SPS-2040) technique in a vacuum. The sintering temperature is 673 K and the holding time is 5 min. The sintering pressure is 40 MPa. In the annealing experiments, the samples were sealed in the quartz tubes with a high vacuum (~10^{-4} Torr, 1 Torr = 133.322 368 4 Pa) and then heated to the assigned temperature. The phase compositions were analyzed by X-ray diffractometer with Cu K_α sources (XRD, D8 Advance, Bruker) and field emission electron microscopy (FESEM, ZEISS, Supra 55) equipped with Energy Dispersive X-ray Spectroscopy (EDS, Oxford, UK). The Vicker Hardness (HV) was measured by using a microhardness tester (hv-1000z) with a load of 0.2 N and a loading time of 10 s. The details about the TE properties [49] and ATP measurements can be found elsewhere [50].

3. Results and discussion

Due to the intrinsic metastability of the cubic δ-phase, the as-prepared $AgSbTe_2$-based compounds usually include lots of Ag-rich or Sb-rich secondary phases. These secondary phases might not only influence the TE properties but also introduce uncertain effects on the stability. Thus, a phase pure $AgSbTe_2$-based compound is critical for investigating the stability at elevated temperatures. For this purpose, herein, we prepared a series of $Ag_xSb_{2-x}Te_{3-x}$ (x = 1.0, 0.9, 0.8 and 0.7) samples by the melt-quenching method. Fig. 2a shows their powder X-ray diffraction (XRD) patterns. The main diffraction peaks can be indexed to the δ-phase with cubic rock salt structure (JCPDS 15–0540) [24]. This proves that the decomposition rate of the δ-phase is slow in the present fabrication process, which could be due to the small decomposition energy difference between the δ-phase (−158 meV/cation) and the Ag_2Te/Sb_2Te_3 mixtures (−172 meV/cation) [37,48]. No obvious extra diffraction peaks are observed in the XRD pattern of $Ag_{0.9}Sb_{1.1}Te_{2.1}$, indicating that it is a single phase on the macroscale. We also prove the phase-pure nature of this composition on the microscale and nanoscale via energy-dispersive spectrometry (EDS) and atom probe tomography (APT), respectively, as will be elaborated below. The diffraction peaks belonging to the Ag_2Te-like structure are observed in the XRD pattern of $AgSbTe_2$. Likewise, the diffraction peaks belonging to the Sb_2Te_3-like structure are observed in the XRD patterns of $Ag_{0.8}Sb_{1.2}Te_{2.2}$ and $Ag_{0.7}Sb_{1.3}Te_{2.3}$. The peak intensities of the Sb_2Te_3-like structure are very weak for $Ag_{0.8}Sb_{1.2}Te_{2.2}$, but strong for $Ag_{0.7}Sb_{1.3}Te_{2.3}$. Thus, the prepared $AgSbTe_2$ is the mixture of cubic δ-phase and Ag_2Te-like structure phase, while $Ag_{0.8}Sb_{1.2}Te_{2.2}$ and $Ag_{0.7}Sb_{1.3}Te_{2.3}$ are the mixtures of cubic δ-phase and Sb_2Te_3-like structure phase.

The phase compositions of $Ag_xSb_{2-x}Te_{3-x}$ (x = 1.0, 0.9, 0.8 and 0.7) samples can be further confirmed by EDS elemental mapping. As shown in Fig. 2b, homogeneous elemental distributions on microscale can be only found in $Ag_{0.9}Sb_{1.1}Te_{2.1}$. In contrast, obvious Ag-rich areas are observed in $AgSbTe_2$, while Sb-rich areas are observed in $Ag_{0.8}Sb_{1.2}Te_{2.2}$ and $Ag_{0.7}Sb_{1.3}Te_{2.3}$. Combining EDS with the XRD analysis, the Ag-rich areas are determined as Ag_2Te, while the Sb-rich areas are determined as Sb_2Te_3 containing a tiny amount of Ag. The actual chemical compositions of the δ-phase in these four $Ag_xSb_{2-x}Te_{3-x}$ samples are listed in Table 1. Those of $Ag_{0.9}Sb_{1.1}Te_{2.1}$ and $Ag_{0.8}Sb_{1.2}Te_{2.2}$ are similar with the nominal chemical compositions, but those of $AgSbTe_2$ and $Ag_{0.7}Sb_{1.3}Te_{2.3}$ are

Table 1
Phase compositions in $Ag_xSb_{2-x}Te_{3-x}$ (x = 1, 0.9, 0.8 and 0.7) samples.

Nominal Schemical composition	Phase compositions	Actual mole fraction (%)		
		Ag	Sb	Te
$AgSbTe_2$	matrix (δ-phase)	22.7	27.3	50.0
	Ag-rich areas	66.7		33.3
$Ag_{0.9}Sb_{1.1}Te_{2.1}$	matrix (δ-phase)	22.0	26.8	51.2
$Ag_{0.8}Sb_{1.2}Te_{2.2}$	matrix (δ-phase)	19.6	28.7	51.7
	Sb-rich areas	2.7	39.2	58.1
$Ag_{0.7}Sb_{1.3}Te_{2.3}$	matrix (δ-phase)	19.8	29.0	51.2%
	Sb-rich areas	1.0	40.4	58.6

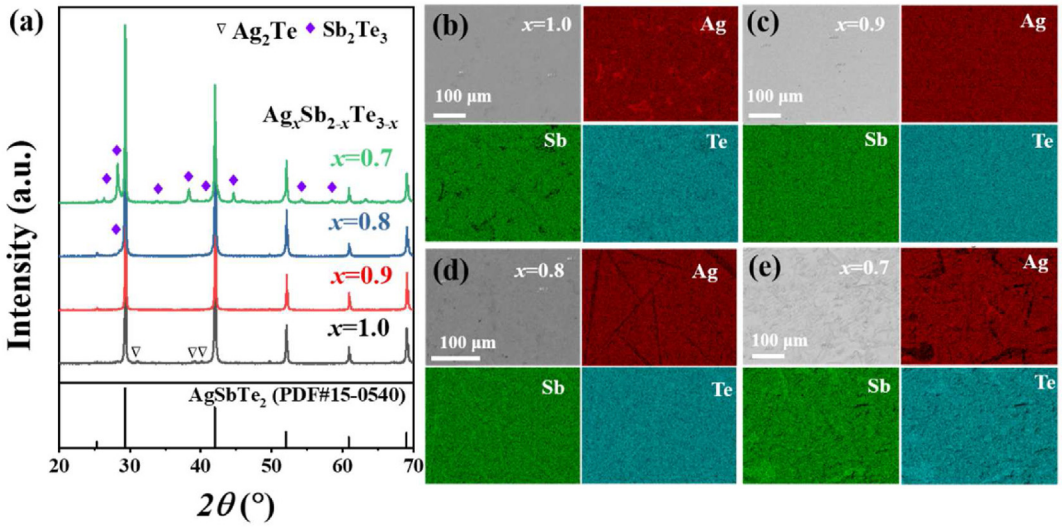

Fig. 2. (a) Powder XRD patterns of $Ag_xSb_{2-x}Te_{3-x}$ (x = 1, 0.9, 0.8 and 0.7) samples. Backscattered electron (BSE) images and energy dispersive X-ray spectroscopy (EDS) elemental mapping for $Ag_xSb_{2-x}Te_{3-x}$ with (b) x = 1; (c) x = 0.9; (d) x = 0.8; and (e) x = 0.7, respectively.

quite different. This is reasonable since $AgSbTe_2$ and $Ag_{0.7}Sb_{1.3}Te_{2.3}$ fall beyond the composition range of the δ-phase defined by Petzow *et al.* (Fig. 1c) [40,41]. However, although both $Ag_{0.9}Sb_{1.1}Te_{2.1}$ and $Ag_{0.8}Sb_{1.2}Te_{2.2}$ fall in the composition range of the δ-phase, the final phase compositions in the prepared products are still different. Based on the Ag_2Te-Sb_2Te_3 phase diagram, the lower temperature limit of cubic δ-phase is about 673 K for $Ag_{0.9}Sb_{1.1}Te_{2.1}$, while about 780 K for $Ag_{0.8}Sb_{1.2}Te_{2.2}$. Thus, during the cooling process, $Ag_{0.8}Sb_{1.2}Te_{2.2}$ has a higher degree of supercooling than $Ag_{0.9}Sb_{1.1}Te_{2.1}$, which would facilitate the nucleation and growth of decomposition products [51]. This is responsible for the formation of Sb-rich areas in $Ag_{0.8}Sb_{1.2}Te_{2.2}$.

It is striking that sample $x = 0.9$ is a pure phase while other compositions show either Ag_2Te ($x > 0.9$) or Sb_2Te_3 ($x < 0.9$) precipitates. The nominal composition of $AgSbTe_2$ shows identical cations and anions. However, this atomic configuration is intrinsically unstable due to the large population of occupied anti-bonding states in the vicinity of the Fermi energy level, as calculated by the crystal orbital Hamilton population (COHP) method [52]. Similar phenomena have been reported in other compounds employing the same metavalent bonding mechanism such as IV-VI rocksalt chalcogenides [53] and Ge-Sb-Te [54]. A typical feature of these systems is that the formation energies of acceptors, *e.g.*, cation vacancies, are very low. The calculated formation energies for the Ag and Sb vacancy in $AgSbTe_2$ are 0.016 eV and 0.344 eV, respectively [52]. In contrast, the formation energy of anion Te vacancy is 1.408 eV [52]. A stoichiometric $AgSbTe_2$ will create cation vacancies spontaneously to depopulate the occupied anti-bonding states and thus stabilize the system, yielding the formation of Ag-deficient $AgSbTe_2$ and Ag_2Te precipitates. In $Ag_{0.9}Sb_{1.1}Te_{2.1}$, the population of occupied anti-bonding states is already reduced by the artificially introduced Ag-deficiency, thus it shows better stability than the stoichiometric $AgSbTe_2$. Yet, the limit of the number of acceptors still exists due to the self-compensation effect. The system simultaneously introduces donors to maintain charge neutrality when increasing the number of acceptors markedly, leading to the formation of defect complexes or precipitates, such as Ag_2Te and Sb_2Te_3.

Given that $Ag_{0.9}Sb_{1.1}Te_{2.1}$ is phase pure at room temperature, we further perform annealing experiments to investigate its decomposition behavior. Fig. 3a shows the XRD patterns of the $Ag_{0.9}Sb_{1.1}Te_{2.1}$ samples after annealing for 12 h at different temperatures (473 K, 498 K, 523 K and 573 K). The patterns for the samples annealed below 498 K are roughly the same as the pattern before annealing. However, obvious diffraction peaks belonging to the Ag_2Te- and Sb_2Te_3-like structures appear when the sample has been annealed at 523 K. When the annealing temperature has reached 573 K, the diffraction peaks belonging to the δ-phase have disappeared completely. The remaining diffraction peaks can be indexed to a mixture of Ag_2Te- and Sb_2Te_3-like structures. This indicates that the δ-phase has decomposed at this annealing step. Similar phenomena have also been observed by Wu *et al.* [44] and Wyżga *et al.* [41] when annealing $AgSbTe_2$ at 523 K for a long duration.

Fig. S1and Fig. 3b show the EDS elemental mapping for the $Ag_{0.9}Sb_{1.1}Te_{2.1}$ after annealing for 12 h at different temperatures. All elements are homogeneously distributed in the sample annealed at 473 K (Fig. S1a). This indicates that there is no significant decomposition upon annealing at this temperature. Slight inhomogeneous element distributions are observed in the sample annealed at 523 K (Fig. S1b). Particularly, as shown in Fig. 3b, two different regions with distinct contrasts are observed in this sample. The stoichiometry in the needle-like areas with bright contrast is close to Ag_2Te, corresponding to the Ag_2Te-like structure determined by the above X-ray analysis. The stoichiometry in other areas with gray contrast is close to $Ag_{10}Sb_{35}Te_{55}$, corresponding to the Sb_2Te_3-like structure determined by the X-ray analysis and confirmed by atomic-scale scanning transmission electron microscopy [46]. The absence of the $Ag_{0.9}Sb_{1.1}Te_{2.1}$ region is consistent with the above X-ray analysis that $Ag_{0.9}Sb_{1.1}Te_{2.1}$ has almost been completely decomposed after annealing at 573 K for 12 h.

In order to rule out the possibility of a slow decomposition rate at a lower temperature, we further perform long-term annealing at 473 K on $Ag_{0.9}Sb_{1.1}Te_{2.1}$. As shown in Fig. 3c, after annealing at this temperature for up to 720 h, the XRD pattern still shows no obvious change compared with the one obtained after annealing for 12 h. Likewise, Fig. 3d shows that all elements are homogeneously distributed inside the matrix without any enrichment after annealing at 473 K for 720 h. No Ag-rich or Sb-rich secondary phases are observed. These results confirm that $Ag_{0.9}Sb_{1.1}Te_{2.1}$ is indeed stable at 473 K. Thus, the above results imply that the decomposition threshold temperature for the $Ag_{0.9}Sb_{1.1}Te_{2.1}$ is above 473 K. At and below this temperature, decomposition does not occur.

The existence of the decomposition threshold of $Ag_{0.9}Sb_{1.1}Te_{2.1}$ can be further confirmed by the measurement of TE properties. Fig. 4a-c shows the Seebeck coefficient (S), electrical conductivity (σ), and power factor (PF) for the $Ag_{0.9}Sb_{1.1}Te_{2.1}$ samples after annealing at different temperatures. These properties are sensitively related to phase distribution in the corresponding sample. Thus, they will be significantly modified if decomposition occurs. As shown in Fig. 4a–c, the S, σ, and PF for the samples annealed at 453 K and 473 K for 12 h are similar to those for the $Ag_{0.9}Sb_{1.1}Te_{2.1}$ sample without annealing. Furthermore, even after annealing at 473 K for 720 h, the S, σ, and PF are still similar to those for the as-prepared sample. The differences are within ±7% for S, σ, and PF. These findings confirm that $Ag_{0.9}Sb_{1.1}Te_{2.1}$ does not decompose after the annealing at 453 K and 473 K. The sample annealed at 498 K has similar σ but smaller S compared to the as-prepared sample. With further increasing the annealing temperature to 523 K and 573 K, the relevant properties, *i.e.* S, σ, and PF are significantly changed. This is in line with the decomposition that takes place at these annealing temperatures. Based on these results, the stable TE performance range of $Ag_{0.9}Sb_{1.1}Te_{2.1}$ is plotted in Fig. 4d. In this range, $Ag_{0.9}Sb_{1.1}Te_{2.1}$ can be stably utilized, as confirmed by the almost overlapped σ and S in the cycling test (Fig. S4).

The above EDS results show elemental distributions on the micrometer scale. Yet, phase separation starts on a smaller length scale, related to the size of the critical nucleus needed to surmount to form a new phase. Hence, we performed APT to characterize the elemental distribution on the sub-nanometer scale [55–57]. The results obtained help us to determine the decomposition mechanism of the $Ag_{0.9}Sb_{1.1}Te_{2.1}$ sample. Fig. 5 shows the elemental distributions of $Ag_{0.9}Sb_{1.1}Te_{2.1}$ characterized by APT. No nano-precipitates are detected, corroborating the phase-pure nature of this composition as prepared. Interestingly, we observed a high number density of planar defects (edge-on view in the figure) inside the matrix as depicted by the iso-composition surfaces of 17% (in mole) Ag and 30% (in mole) Sb (Fig. 5a). These planar defects are consistent with the stacking faults characterized by transmission electron microscopy (TEM) [46]. The distance between two adjacent stacking faults ranges from 10 nm to 30 nm. The chemical width of each stacking fault is around 1 nm. The linear composition profile across these stacking faults (Fig. 5c) indicates their Ag-deficient and Sb-enrichment feature in agreement with Cojocaru-Mirédin *et al.* [46]. The stoichiometry of the matrix between stacking faults is very close to the nominal composition of $Ag_{0.9}Sb_{1.1}Te_{2.1}$. Combining the previous microstructures revealed by TEM with the present APT compositions, these stacking faults are

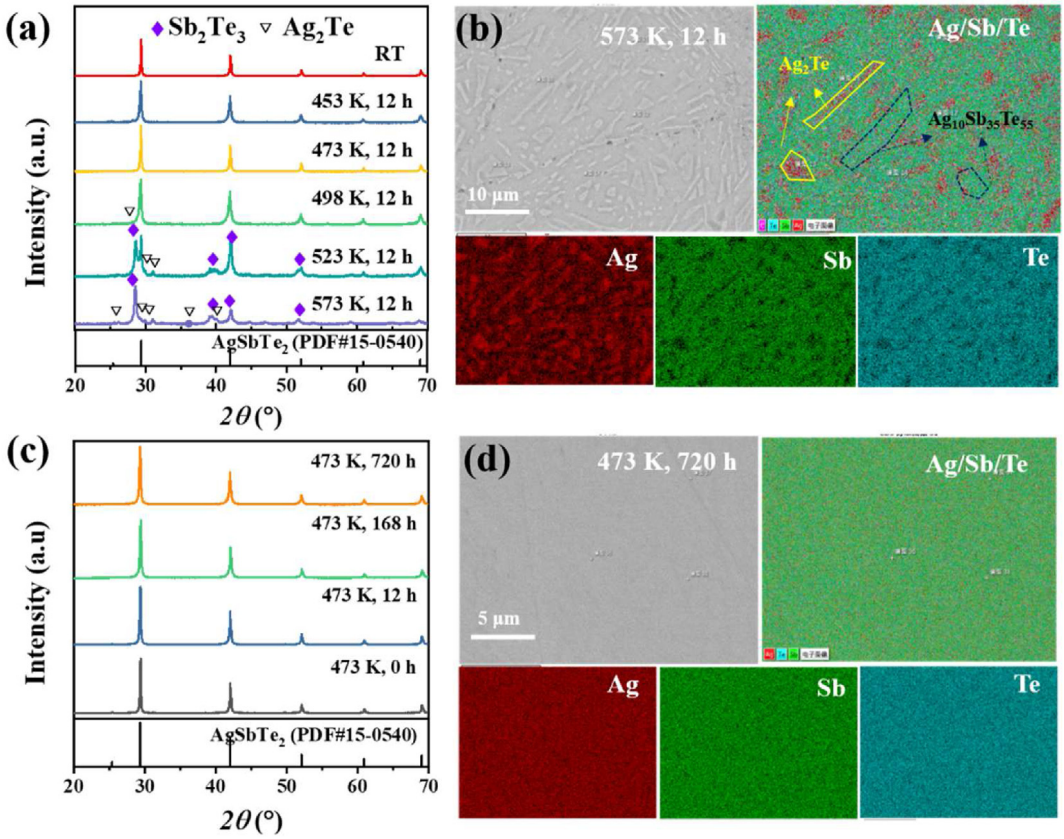

Fig. 3. (a) XRD patterns for $Ag_{0.9}Sb_{1.1}Te_{2.1}$ after annealing for 12 h at different temperatures (473 K, 498 K, 523 K and 573 K). (b) BSE image and EDS elemental mapping for $Ag_{0.9}Sb_{1.1}Te_{2.1}$ after annealing for 12 h at 573 K. (c) XRD patterns for $Ag_{0.9}Sb_{1.1}Te_{2.1}$ after annealing at 473 K for different durations (0 h, 12 h, 168 h and 720 h). (d) BSE image and EDS elemental mapping for $Ag_{0.9}Sb_{1.1}Te_{2.1}$ after annealing at 473 K for 720 h.

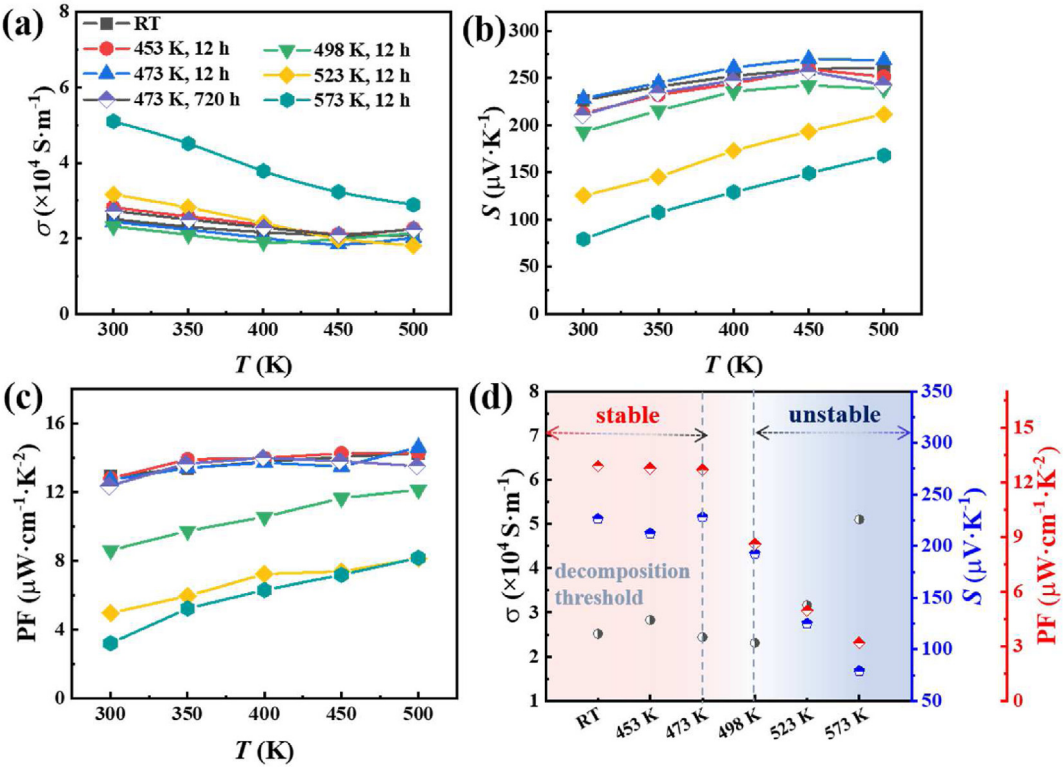

Fig. 4. (a) Electrical conductivity (σ), (b) Seebeck coefficient (S), and (c) power factor (PF) for the $Ag_{0.9}Sb_{1.1}Te_{2.1}$ samples after annealing 12 h at different temperatures (453 K, 473 K, 498 K, 523 K, and 573 K). The data after annealing at 473 K for 720 h are also included. (d) Room-temperature S, σ, and PF as a function of annealing temperature. The stable and unstable temperature windows are plotted for $Ag_{0.9}Sb_{1.1}Te_{2.1}$.

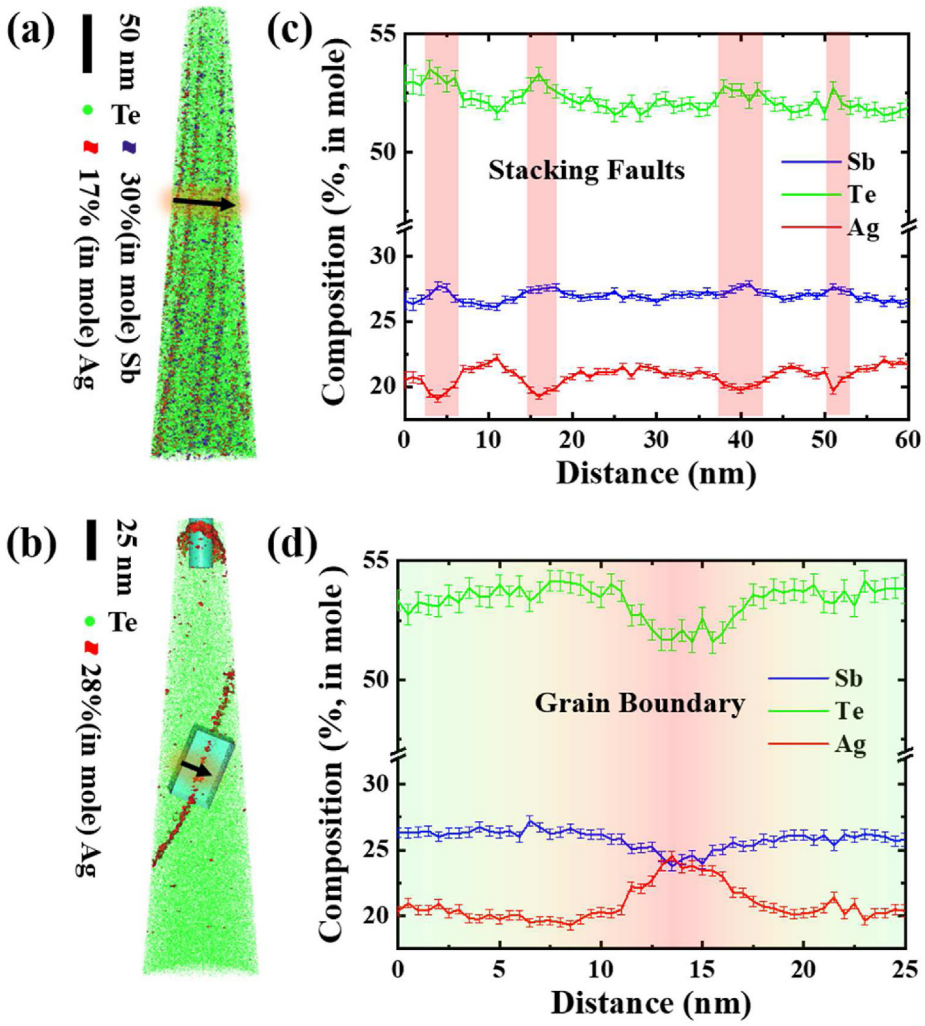

Fig. 5. Three-dimensional atom probe tomography (3D-APT) maps for $Ag_{0.9}Sb_{1.1}Te_{2.1}$ without annealing at two different areas to illustrate the elemental distributions near (a) planar stacking faults and (b) grain boundary. Linear concentration profiles of Ag (red), Sb (blue), and Te (green) across the (c) planar stacking faults and (d) grain boundary as indicated by the black arrows in (a–b).

related to the double-Te layers [58,59]. In contrast to the Ag-deficient feature at stacking faults, we observed Ag-enrichment at one curved individual planar defect (edge-on view in the figure) which should be a grain boundary (GB) given the distinct number density and composition of stacking faults, as highlighted by the Ag-rich isosurface in Fig. 5b. The linear composition profile across the GB within a cuboid region of interest (Fig. 5d) indicates Ag enrichment and Sb/Te depletion at the GB area. Besides the chemical composition information, APT also detected an abnormal bond-breaking behavior for this material, showing an unusually high probability to form several distinct fragments upon a single successful laser pulse, named "probability of multiple events" (PME = 75%). This large PME value is a hallmark of MVB compounds [60], corroborating the unconventional chemical bonding mechanism of $Ag_{0.9}Sb_{1.1}Te_{2.1}$. Given the unique property portfolio of MVB compounds that enables outstanding TE performance [61], the high PME value is a direct indicator of remarkable TE materials.

According to the classic nucleation theory, the critical nucleation radius for heterogeneous nucleation is much smaller than that for homogeneous nucleation. The stacking faults and grain boundaries characterized by APT provide heterogeneous nuclei. The Ag-enrichment and Sb-enrichment feature at the GB and stacking fault, respectively, is indicative of the embryo of the secondary phase. This could explain the Ag_2Te precipitates surrounding GBs observed in $AgSbTe_2$ by Lee *et al.* [62]. Cojocaru-Mirédin *et al.* [46] observed a high number density of stacking faults in the as-quenched $AgSbTe_2$ but mainly $(Ag,Sb)_2Te_3$ secondary phase in the sample after annealing at 380 °C for 192 h. This is indirect evidence that the stacking faults could be the precursors of Sb_2Te_3 precipitates. More proofs should be given by in-situ experiments and could be interesting for future work.

Comparing with other $Ag_xSb_{2-x}Te_{3-x}$ (x = 1.0, 0.8, and 0.7) samples, $Ag_{0.9}Sb_{1.1}Te_{2.1}$ has not only the highest phase purity, but also the best TE performance. Fig. 6 shows the TE properties of $Ag_xSb_{2-x}Te_{3-x}$ from 300 K to 500 K. The flexion around 400 K in the S curve of $AgSbTe_2$ is caused by the monoclinic-cubic phase transition of Ag_2Te, as confirmed by the existence of one endothermic peak near this temperature in the heat flow curve of $AgSbTe_2$ (Fig. S5) [63]. With decreasing x, the σ is gradually increased (Fig. 6a), while the S is decreased (Fig. 6b) over the entire temperature range. In the δ-phase, the number of cations (Ag and Sb) is less than that of anions (Te), yielding the existence of cation vacancies inside the cubic structure. These cation vacancies act as acceptors to provide extra holes, resulting in the p-type conduction

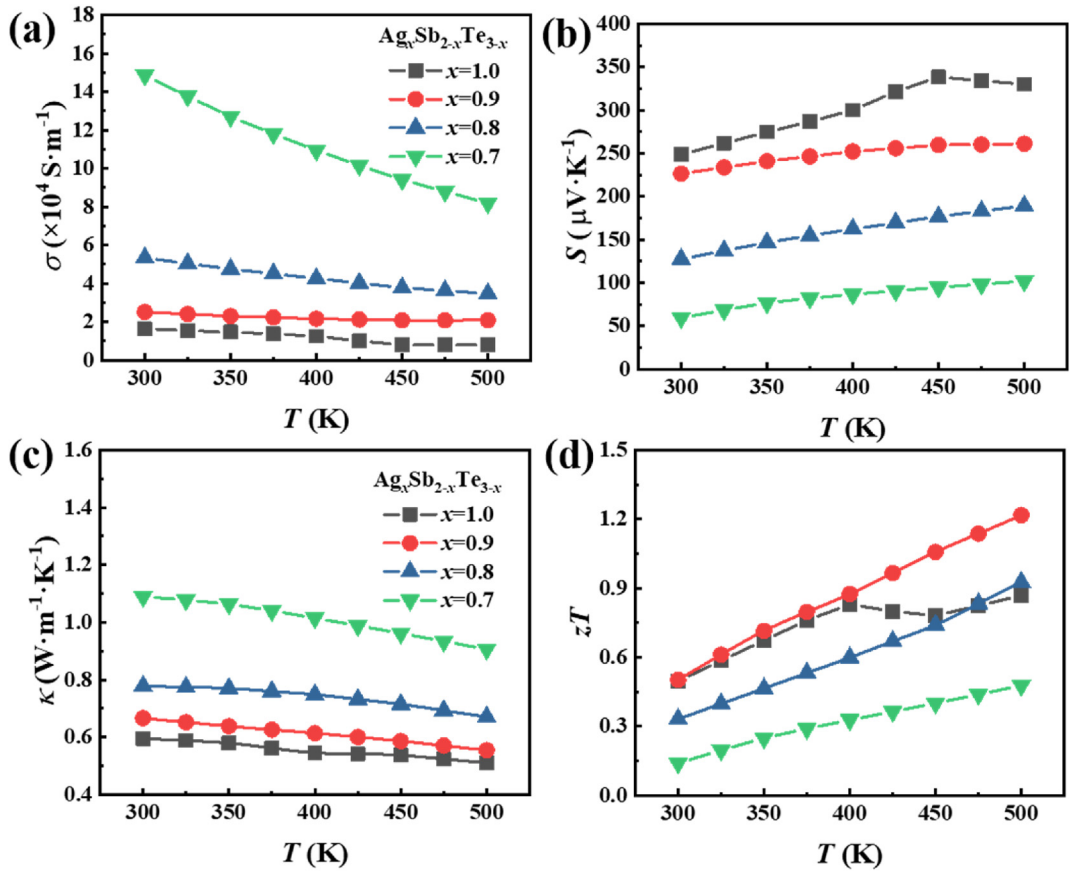

Fig. 6. Temperature-dependent (a) Seebeck coefficient (S), (b) electrical conductivity (σ), (c) thermal conductivity (κ), and (d) TE figure of merit (zT) for $Ag_xSb_{2-x}Te_{3-x}$ (x = 1.0, 0.9, 0.8, and 0.7) samples.

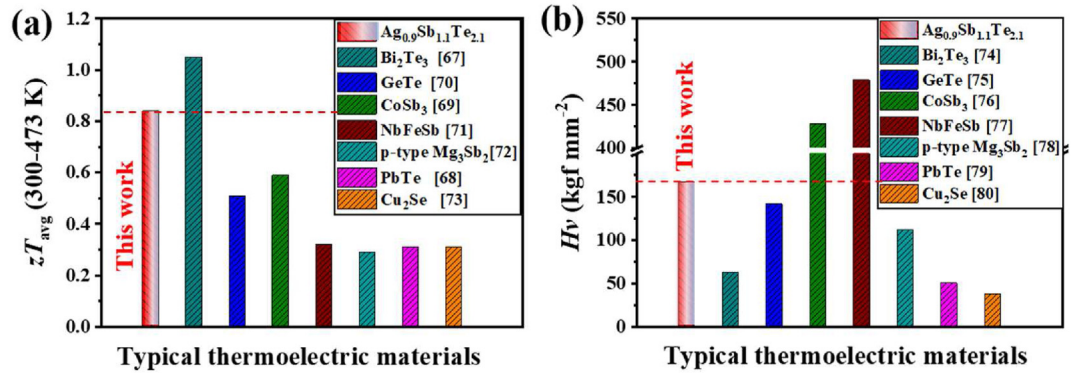

Fig. 7. Comparisons on the (a) average zT (zT_{avg}) between 300 and 475 K and (b)Vickers hardness for $Ag_{0.9}Sb_{1.1}Te_{2.1}$ and several typical TE materials. The zT data are taken from references [67–73]. The Vickers hardness data are taken from references [74–80].

and positive S [28]. With decreasing the x in $Ag_xSb_{2-x}Te_{3-x}$, the number of cation vacancies is increased, which is the main reason for the increased σ and the decreased S. Unfortunately, the carrier concentration of $AgSbTe_2$-based compounds is very difficult to be accurately measured due to the existence of highly mobile electrons that dominate the Hall measurements [43,64,65]. Based on the Goldsmid and Sharp's formula [66], the band gap (E_g) of $Ag_{0.9}Sb_{1.1}Te_{2.1}$ is estimated to be around 0.25 eV, which is slightly lower than the measured optical band gap for $AgSbTe_2$ [23,36]. Fig. S2 shows that $Ag_{0.9}Sb_{1.1}Te_{2.1}$ has the highest power factor (PF = 14.2 $\mu W \cdot cm^{-1} \cdot K^{-2}$) among these four samples. The thermal conductivity (κ) also increases with increasing the x (Fig. 6c), which is mainly attributed to the increased contribution from charge carriers (Fig. S3). Finally, Fig. 6d presents that the zT of $Ag_{0.9}Sb_{1.1}Te_{2.1}$ is the highest among these samples. Its zT is about 0.5 at 300 K and 1.1 at 475 K. As shown in Fig. 1b, this zT value can be still largely improved by doping external elements, such as Cd [39], Zn [34] and Se [22].

Generally, the maximum zT of $AgSbTe_2$-based ternary chalcogenides appears at the temperature range 500–700 K, such as zT = 2.1 at 573 K for $AgSbTe_{1.85}Se_{0.15}$ [22], zT = 2.6 at 573 K for $AgSb_{0.94}Cd_{0.06}Te_2$ [39], zT = 1.9 at 585 K for $AgSb_{0.96}Zn_{0.04}Te_2$ [34],

and $zT = 1.35$ at 650 K for $Ag(Sb_{0.93}In_{0.07})Te_2$ (Fig. 1b). Being limited by the decomposition temperature, the present zT of $Ag_{0.9}Sb_{1.1}Te_{2.1}$, 1.1 at 475 K, is lower than these zTs. However, it should be noted that this zT value is obtained in the stable temperature range of $Ag_{0.9}Sb_{1.1}Te_{2.1}$. Furthermore, this zT value is already much higher than most of the other TE materials in a comparable temperature range. Fig. 7a plots the average zT (zT_{avg}) between 300 and 475 K for $Ag_{0.9}Sb_{1.1}Te_{2.1}$ and several typical TE materials. The zT_{avg} is 0.84 for $Ag_{0.9}Sb_{1.1}Te_{2.1}$. This value is lower than that of the best room-temperature TE material, *i.e.* Bi_2Te_3-alloys [67], but it is much higher than other TE materials (*e.g.* PbTe [68], skutterudites [69], and GeTe [70]) in the same temperature range [71–73]. In addition, Fig. 7b shows that the Vickers hardness of $Ag_{0.9}Sb_{1.1}Te_{2.1}$ is much higher than that for Bi_2Te_3-alloys, indicating that it has a better ability to withstand the external mechanical stress or vibrations [74–80]. Thus, $Ag_{0.9}Sb_{1.1}Te_{2.1}$ has considerable potential for applications in miniaturized refrigeration and power generation in the low- and middle-temperature ranges.

4. Conclusions and outlook

In this work, the means have been explored to improve the stability of $AgSbTe_2$-based ternary chalcogenides. Phase pure $Ag_{0.9}Sb_{1.1}Te_{2.1}$ stands out from a series of $Ag_xSb_{2-x}Te_{3-x}$ samples for the stability and TE performance investigations. The results indicate that the decomposition threshold of $Ag_{0.9}Sb_{1.1}Te_{2.1}$ appears around 473 K. Below this threshold, $Ag_{0.9}Sb_{1.1}Te_{2.1}$ has quite good stability, exhibiting scarcely changed chemical compositions and TE properties after long-term annealing (720 h at 473 K). The zT of $Ag_{0.9}Sb_{1.1}Te_{2.1}$ at 475 K is 1.1, which is superior to most other TE materials in a comparable temperature range. Combining the good stability below the decomposition threshold, high zT_{avg} at 300–475 K, and good mechanical performance, $Ag_{0.9}Sb_{1.1}Te_{2.1}$ is a competitive TE material for applications in miniaturized refrigeration and power generation near room temperature. Besides, APT results provide an important hint that the Ag-rich grain boundaries and Sb-rich stacking faults could be embryos for heterogeneous nucleation and thus accelerate the decomposition of the compound. Eliminating these defects or inhibiting the segregation of Ag to grain boundaries by doping could be an effective way to further stabilize the compound.

Declaration of competing interest

The authors declare that they have no known competing financial interests or personal relationships that could have appeared to influence the work reported in this paper.

Acknowledgements

This work is supported by the National Natural Science Foundation of China (91963208 and 52122213), Shanghai Government (20JC1415100), Shanghai Pilot Program for Basic Research-Chinese Academy of Science, Shanghai Branch (JCYJ-SHFY-2022-002), and the CAS-DOE Program of Chinese Academy of Sciences (121631KYSB20180060). Y. Yu, O. Cojocaru-Mirédin and M. Wuttig acknowledge the financial support from DFG SFB 917 project. Y. Yu acknowledges the financial support under the Excellence Strategy of the Federal Government and the Länder within the ERS RWTH Start-Up grant (Grant No. StUpPD_392–21).

Appendix A. Supplementary data

Supplementary data to this article can be found online at https://doi.org/10.1016/j.jmat.2022.07.005.

References

[1] Yang Q, Qiu P, Shi X, Chen LD. J Inorg Mater 2021;36(4):347–54. http://www.jim.org.cn/EN/10.15541/jim20200417.
[2] Peng LM, Yang SQ, Wei T-R, Qiu PF, Yang J, Zheng Z, Shi X, Chen LD. J Materiomics 2022;8:656–61. https://doi.org/10.1016/j.jmat.2021.11.007.
[3] Wu Y, Lou Q, Qiu Y, Guo J, Mei Z-Y, Xu X, Feng J, He JQ, Ge Z-H. Inorg Chem Front 2019;6(6):1374–81. https://doi.org/10.1039/C9QI00213H.
[4] Deng T, Xing T, Brod MK, Sheng Y, Qiu P, Veremchuk I, Song Q, Wei T, Yang J, Snyder G, Grin Y, Chen L. Energy Environ Sci 2020;13(9):3041–53. https://doi.org/10.1039/D0EE02209H.
[5] Liang J, Wang T, Qiu P, Yang S, Ming C, Chen H, Song Q, Wei T-R, Ren D, Sun Y-Y, Shi X, He J, Chen L. Energy Environ Sci 2019;12(10):2983–90. https://doi.org/10.1039/C9EE01777A.
[6] Jiang B, Yu Y, Cui J, Liu X, Liao J, Zhang Q, Huang Y, Ning S, Jia B, Zhu B, Bai S, Chen L, Pennycook JS, He J. Science 2021;371(6531):830–4. https://doi.org/10.1126/science.abe1292.
[7] Gayner C, Kar KK. Prog Mater Sci 2016;83:330–82. https://doi.org/10.1016/j.pmatsci.2016.07.002.
[8] Mao J, Chen G, Ren Z. Nat Mater 2021;20(4):454–61. https://doi.org/10.1038/s41563-020-00852-w.
[9] Qiu P, Cheng J, Chai J, Du X, Xia X, Ming C, Zhu C, Yang J, Sun Y-Y, Xu F, Shi X, Chen L. Adv Energy Mater 2022:2200247. https://doi.org/10.1002/aenm.202200247.
[10] Li J, Liu R, Song Q, Gao Z, Huang H, Zhang Q, Shi X, Bai S, Chen L. Acta Mater 2022;224:117526. https://doi.org/10.1016/j.actamat.2021.117526.
[11] Shang H, Liang Z, Xu C, Song S, Huang D, Gu H, Mao J, Ren Z, Ding F. Acta Mater 2020;201:572–9. https://doi.org/10.1016/j.actamat.2020.10.035.
[12] Mao T, Qiu P, Hu P, Du X, Zhao K, Wei T-R, Xioa J, Shi X, Chen L. Adv Sci 2020;7(1):1901598. https://doi.org/10.1002/advs.201901598.
[13] Xing T, Song Q, Qiu P, Zhang Q, Xia X, Liao J, Liu R, Yang J, Bai S, Ren D, Shi X, Chen L. Natl Sci Rev 2019;6(5):944–54. https://doi.org/10.1093/nsr/nwz052.
[14] Ghosh T, Roychowdhury S, Dutta M, Biswas K. ACS Energy Lett 2021;6(8):2825–37. https://doi.org/10.1021/acsenergylett.1c01184.
[15] Geller S, Wernick JH. Acta Crystallogr 1959;12(1):46–54. https://doi.org/10.1107/S0365110X59000135.
[16] Kooi BJ, Wuttig M. Adv Mater 2020;32(21):1908302. https://doi.org/10.1002/adma.201908302.
[17] Raty JY, Schumacher M, Golub P, Deringer VL, Gatti C, Wuttig M. Adv Mater 2019;31(3):1806280. https://doi.org/10.1002/adma.201806280.
[18] Guarneri L, Jakobs S, von Hoegen A, Maier S, Xu M, Zhu M, Wahl S, Teichrib C, Zhou Y, Cojocaru-Mirédin O, Raghuwanshi M, Schön CH, Drögeler M, Stampfer C, M PS, Lobo R, Piarristeguy A, Pradel A, Raty J-Y, Wuttig M. Adv Mater 2021;33(39):2102356. https://doi.org/10.1002/adma.202102356.
[19] Wuttig M, Deringer VL, Gonze X, Bichara C, Raty J-Y. Adv Mater 2018;30(51):1803777. https://doi.org/10.1002/adma.201803777.
[20] Yu Y, Cagnoni M, Cojocaru-Mirédin O, Wuttig M. Adv Funct Mater 2020;30(8):1904862. https://doi.org/10.1002/adfm.201904862.
[21] Zayed HA, Ibrahim AM, Soliman LI. Vacuum 1996;47(1):49–51. https://doi.org/10.1016/0042-207X(95)00184-0.
[22] Hong M, Chen ZG, Yang L, Miao Z-M, Zou Y-C, Chen Y-H, Matsumura S, Zou J. Adv Energy Mater 2018;8(9):1702333. https://doi.org/10.1002/aenm.201702333.
[23] Morelli DT, Jovovic V, Heremans JP. Phys Rev Lett 2008;101(3):035901. https://doi.org/10.1103/PhysRevLett.101.035901.
[24] Wu H, Chen S, Ikeda T, Snyder G. J. Acta Mater 2012;60(17):6144–51. https://doi.org/10.1016/j.actamat.2012.07.057.
[25] Irie T. J Phys Soc Jpn 1962;17(11):1810–1. https://doi.org/10.1143/JPSJ.17.1810.
[26] Irie T, Takahama T, Ono T. J Phys Soc Jpn 1963;2(2):72. https://doi.org/10.1143/JJAP.2.72.
[27] Ma J, Delaire O, May AF, Carlton CE, McGuire MA, VanBebber LH, Abernathy DL, Ehlers G, Hong T, Huq A, Tian W, Keppens VM, Shao-Horn Y, Sale BC. Nat Nanotechnol 2013;8(6):445–51. https://doi.org/10.1038/nnano.2013.95.
[28] Ye LH, Hoang K, Freeman AJ, Mahanti SD, He J, Tritt TM, Kanatzidis MG. Phys Rev B 2008;77(24):245203. https://doi.org/10.1103/PhysRevB.77.245203.
[29] Jovovic V, Heremans JP. J Electron Mater 2009;38(7):1504–9. https://doi.org/10.1007/s11664-009-0669-7.
[30] Wang H, Li JF, Zou M, Sui T. Appl Phys Lett 2008;93(20):202106. https://doi.org/10.1063/1.3029774.
[31] Su T, Jia X, Ma H, Yu F, Tian Y, Zuo G, Zheng Y, Jiang Y, Dong D, Deng L, Qin B, Zheng S. J Appl Phys 2009;105(7):073713. https://doi.org/10.1063/1.3106102.
[32] Xu J, Li H, Du B, Tang X, Zhang Q, Uher C. J Mater Chem 2010;20(29):6138–43. https://doi.org/10.1039/C0JM00138D.
[33] Wu Y, Liang Q, Zhao X, Wu H, Zi P, Tao Q, Yu L, Su X, Wu J, Chen Z, Zhang Q, Tang X. ACS Appl Mater Interfaces 2022;14(2):3057–65. https://doi.org/10.1021/acsami.1c21252.
[34] Roychowdhury S, Panigrahi R, Perumal S, Perunal S, Biswas K. ACS Energy Lett 2017;2(2):349–56. https://doi.org/10.1021/acsenergylett.6b00639.
[35] Du B, Li H, Xu J, Tang X, Uher C. Chem Mater 2010;22(19):5521–7. https://doi.org/10.1021/cm101503y.
[36] Mohanraman R, Sankar R, Boopathi KM, Chou FC, Chu CW, Lee CH, Chen YY. J Mater Chem 2014;2(8):2839–44. https://doi.org/10.1039/C3TA14547F.

[37] Lee JK, Ryu B, Park S, Son JH, Park J, Jang J, Oh MW, Park SD. Acta Mater 2022;222:117443. https://doi.org/10.1016/j.actamat.2021.117443.
[38] Mohanraman R, Sankar R, Chou FC, Lee C-H, Lizuka Y, Muthuselvam IP, Chen Y-Y. Apl Mater 2014;2(9):096114. https://doi.org/10.1063/1.4896435.
[39] Roychowdhury S, Ghosh T, Arora R, Xie L, Singh NK, Soni A, He J, WWanghmare U, Biswas K. Science 2021;371(6530):722–7. https://doi.org/10.1126/science.abb3517.
[40] Petzow G, Effenberg G. Ternary alloys. Ternary alloys 1998;2:554.
[41] Wyzga PM, Wojciechowski KT. J Electron Mater 2016;45(3):1548–54. https://doi.org/10.1007/s11664-015-4102-0.
[42] Sugar JD, Medlin DL. J Alloys Compd 2009;478(1–2):75–82. https://doi.org/10.1016/j.jallcom.2008.11.054.
[43] Du B, Yan Y, Tang X. J Electron Mater 2015;44(6):2118–23. https://doi.org/10.1007/s11664-015-3682-z.
[44] Wu HJ, Chen SW. Acta Mater 2011;59(16):6463–72. https://doi.org/10.1016/j.actamat.2011.07.010.
[45] Schmidt M, Wojciechowski KT. AIP Conf Proc 2012;1449(1):175–8. https://doi.org/10.1063/1.4731525.
[46] Cojocaru-Mirédin O, Abdellaoui L, Nagli M, Zhang S, Yu Y, Scheu C, Raabe D, Wuttig M, Amouya Y. ACS Appl Mater Interfaces 2017;9(17):14779–90. https://doi.org/10.1021/acsami.7b00689.
[47] Wyżga P, Veremchuk I, Burkhardt U, Simon P, Grin Y, Wojcihowaki KT. Appl Sci 2018;8(1):52. https://doi.org/10.3390/app8010052.
[48] Hua X, Hegde IV, Wolverton C. Chem Mater 2019;31(22):9445–52. https://doi.org/10.1021/acs.chemmater.9b03318.
[49] Deng T, Qiu P, Xing T, Zhou Z, Wei TR, Ren D, et al. J Mater Chem 2021;9(12):7946–54. https://doi.org/10.1039/D0TA12042A.
[50] An D, Wang J, Zhang J, Zhai X, Kang Z, Fan W, Yan J, Liu Y, Lu L, Jia C-L, Wuttig M, Cojocaru-Mirédin O, Chen S, Wang W, Snyder GJ, Yu Y. Energy Environ Sci 2021;14(10):5469–79. https://doi.org/10.1039/D1EE01977E.
[51] Yu Y, Lv L, Wang X, Zhu B, Huang Z-Y, Zu F-Q. Mater Des 2015;88:743–50. https://doi.org/10.1016/j.matdes.2015.09.074.
[52] Shinya H, Masago A, Fukushima T, Katayama-Yoshida H. Jpn J Appl Phys 2016;55(4):041801. https://doi.org/10.7567/JJAP.55.041801.
[53] Waghmare UV, Spaldin NA, Kandpal HC, Seshadri R. Phys Rev B 2003;67(12):125111. https://doi.org/10.1103/PhysRevB.67.125111.
[54] Wuttig M, Lüsebrink D, Wamwangi D, Wełnic W, Gilleßen M, Dronskowski R. Nat Mater 2007;6(2):122–8. https://doi.org/10.1038/nmat1807.
[55] Gault B, Chiaramonti A, Cojocaru-Mirédin O, Stender P, Dubosq R, Freysoldt C, Makineni AK, Li T, Moody M, Cairney JM. Nat Rev Methods Primers 2021;1(1):1–30. https://doi.org/10.1038/s43586-021-00047-w.
[56] Yu Y, Zhou C, Zhang S, Zhu M, Wuttig M, Scheu C, Raabe D, Snyder GJ, Gault B, Cojocaru-Mirédin O. Mater Today 2020;32:260–74. https://doi.org/10.1016/j.mattod.2019.11.010.
[57] Rodenkirchen C, Cagnoni M, Jakobs S, Cheng Y, Keutge J, Yu Y, Wuttig M, Cojocaru-Mirédin O. Adv Funct Mater 2020;30(17):1910039. https://doi.org/10.1002/adfm.201910039.
[58] Sugar JD, Medlin DL. J Mater Sci 2011;46(6):1668–79. https://doi.org/10.1007/s10853-010-4984-4.
[59] Abdellaoui L, Zhang S, Zaefferer S, Bueno-Villoro R, Baranovskiy A, Cojocaru-Mirédin O, Yu Y, Amouyalal Y, Raabe D, Snyder GJ, Scheu C. Acta Mater 2019;178:135–45. https://doi.org/10.1016/j.actamat.2019.07.031.
[60] Zhu M, Cojocaru-Mirédin O, Mio AM, Keutgen J, Küpers M, Yu Y, Cho J-Y, Dronskowski R, Wuttig M. Adv Mater 2018;30(18):1706735. https://doi.org/10.1002/adma.201706735.
[61] Yu Y, Cagnoni M, Cojocaru-Mirédin O, Wuttig M. Adv Funct Mater 2020;30(8):1904862. https://doi.org/10.1002/adfm.201904862.
[62] Lee JK, Oh MW, Ryu B, Lee JE, Kim B-S, Min B-K, Joo S-J, Lee H-W, Park S-D. Sci Rep-UK 2017;7(1):1–8. https://doi.org/10.1038/s41598-017-04885-1.
[63] Ragimov SS, Aliev SA. Inorg Mater 2007;43(11):1184–6. https://doi.org/10.1134/S0020168507110052.
[64] Jovovic V, Heremans JP. Phys Rev B 2008;77(24):245204. https://doi.org/10.1103/PhysRevB.77.245204.
[65] Goldsmid HJ, Sharp JW. J Electron Mater 1999;28(7):869–72. https://doi.org/10.1007/s11664-999-0211-y.
[66] Li K, Li Z, Yang L, Xiao C, Xie Y. Inorg Chem 2019;58(14):9205–12. https://doi.org/10.1021/acs.inorgchem.9b00852.
[67] Deng R, Su X, Zheng Z, Liu W, Yan Y, Zhang Q, Dravid VP, Uher C, Kanatzidis MG, Tang X. Sci Adv 2018;4(6):eaar5606. https://doi.org/10.1126/sciadv.aar5606.
[68] Heremans JP, Jovovic V, Toberer ES, Saramat A, Kurosaki K, Charoenphakdee A, Yamanaka S, Snyder GJ. Science 2008;321(5888):554–7. https://doi.org/10.1126/science.1159725.
[69] Shi X, Yang J, Salvador JR, Chi M, Cho JY, Wang H, Bai S, Yang J, Zhang W, Chen L. J Am Chem Soc 2011;133(20):7837–46. https://doi.org/10.1021/ja111199y.
[70] Xing T, Zhu C, Song Q, Huang H, Xiao J, Ren D, Shi M, Qiu P, Shi X, Xu F, Chen L. Adv Mater 2021;33(17):2008773. https://doi.org/10.1002/adma.202008773.
[71] Fu C, Bai S, Liu Y, Tang Y, Chen L, Zhao X, Zhu T. Nat Commun 2015;6(1):1–7. https://doi.org/10.1038/ncomms9144.
[72] Ren Z, Shuai J, Mao J, Zhu Q, Song S, Ni Y, Chen S. Acta Mater 2018;143:265–71. https://doi.org/10.1016/j.actamat.2017.10.015.
[73] Liu H, Shi X, Xu F, Zhang L, Zhang W, Chen L, Qiang Li, Uher C, Day T, Snyder GJ. Nat Mater 2012;11(5):422–5. https://doi.org/10.1038/nmat3273.
[74] Perumal S, Roychowdhury S, Biswas K. Inorg Chem Front 2016;3(1):125–32. https://doi.org/10.1039/C5QI00230C.
[75] Wang DZ, Liu WD, Li M, Yin L-C, Gao H, Sun Q, Wu H, Wang Y, Shi X-L, Yang X, Liu Q, Chen Z-G. Chem Eng J 2022:136131. https://doi.org/10.1016/j.cej.2022.136131.
[76] Dahal T, Gahlawat S, Jie Q, Dahal K, Lan Y, White K, Ren Z. J Appl Phys 2015;117(5):055101. https://doi.org/10.1063/1.4906954.
[77] Yan J, Liu F, Ma G, Gong B, Zhu J, Wang X, Ao W, Zhang C, Li Y, Li J. Scripta Mater 2018;157:129–34. https://doi.org/10.1016/j.scriptamat.2018.08.008.
[78] Li J, Zhang S, Jia F, Zheng S, Shi X, Jiang D, Wang S, Lu G, Wu L, Chen Z-G. Mater Today Phys 2020;15:100269. https://doi.org/10.1016/j.mtphys.2020.100269.
[79] Ni JE, Case ED, Khabir KN, Stewart R, Wu C-I, Hogan TP, Timm EJ, Girard SN, Kanatzidis MG. Mater Sci Eng B 2010;170(1–3):58–66. https://doi.org/10.1016/j.mseb.2010.02.026.
[80] Islam SMKN, Li M, Aydemir U, Shi X, Chen L, Snyder GJ, et al. J Mater Chem 2018;6(38):18409–16. https://doi.org/10.1039/C8TA05455J.

Yi Wu received his B.S. in materials science and engineering from Kunming University of Science and Technology. He is currently studying for a Master degree at Shanghai Institute of Ceramics, Chinese Academy of Sciences (SICCAS). His current research mainly focuses on $AgSbTe_2$-based thermoelectric materials.

Pengfei Qiu is a professor at SICCAS. He received his Ph.D. degree in Materials Chemistry and Physics from Shanghai Institute of Ceramics, Chinese Academy of Sciences in 2011 and Bachelor's degree BS in Materials science and Engineering from Wuhan University of Technology in 2006. His research interests are in advanced thermoelectric semiconductors, from synthesizing the materials to understanding the underlying physics and chemistry.

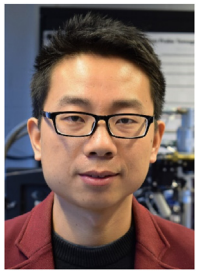

Yuan Yu received his Ph.D. degree in materials science and engineering from Hefei University of Technology in 2017. He was a visiting student at the Institute of Physics (IA) of RWTH Aachen University from November 2015 to May 2017. He then joined Prof. Matthias Wuttig's group as a postdoctoral researcher since 2018. His primary scientific interests include the design of thermoelectric materials by understanding their chemical bonding mechanisms (Metavalent Bonding), as well as the characterization of thermoelectric materials using (transmission) electron back-scatter diffraction and atom probe tomography.